NanoSmart is a European project and plans to design, model, fabricate and validate operation of a new generation of electronic smart systems based on carbon nanotubes (CNT) and 2D material semiconducting electronics. The envisaged platform will have the potential to support future frequency up-scaling, lower power consumption, high operating accuracy by real time ambient sensing and compensation, reconfigurable transmit receive (Rx/Tx) systems that are needed to keep the information age boom in mobile communications and IoT.

NanoSmart develops unique concepts already proven by the consortium such as deep sub-wavelength antennae, CNT NEMS for RF switching, nano electromechanical reconfigurable filters and multiple FET technologies. Monolithic integration of all technologies mentioned above will provide a compact platform including new amplifier architecture, power management, RF switching and antennae on one monolithically integrated chip. Within the front-end IC, three sensor types (Temperature humidity and RF radiation built from novel technology) will also be integrated to provide smart, autonomous system reaction and thus improve accuracy, power efficiency and real-time system health monitoring and on-the-fly response to ambient conditions. The two demonstrators planned are aiming at high-end radar and mass market IoT applications providing this level of smart functionality for the first time.

NanoSmart encompasses extensive design, modelling and advanced characterization techniques to provide the tools for fast industrial take-up of the developed technology. The project's interdisciplinary consortium is made up of 10 partners from 7 countries with a wide geographical spread (France, Sweden, Ireland, Italy, Romania, Greece, and Spain) and includes a global industrial player, two SMEs and top EU academic and research institutions.

This NanoSmart newsletter intends to present the latest progress obtained during first year of the project.

Design and Simulation activities

➢ CNTs Antenna

Concerning antenna design, NANOSMART consortium innovation relies on the success of implementation of graphene layer in an integrated MWCNT-based emitting device at final demonstrator working frequency in the X-band.

$$\boldsymbol{\sigma(\omega,\mu_c,\Gamma,T)} = j\frac{e^2 k_B T}{\pi\hbar}(\omega - j2\Gamma)\left[\frac{1}{(\omega-j2\Gamma)^2}\int_0^\infty \varepsilon\left(\frac{\partial f_d(\varepsilon)}{\partial\varepsilon} - \frac{\partial f_d(-\varepsilon)}{\partial\varepsilon}\right)d\varepsilon\right] - \int_0^\infty \frac{f_d(-\varepsilon)-f_d(\varepsilon)}{(\omega-j2\Gamma)^2-4\left(\frac{\varepsilon}{\hbar}\right)^2}d\varepsilon \qquad (1)$$

A completed electromagnetic analysis of electromagnetic material properties from mono/multi layered graphene sheet layer is mandatory. Starting from basic graphene properties in electromagnetic conductivity from Kubo formula in microwave domain and electrons kinetic transport in such a material (1), complex inductive behaviour can be formulated. ESPCI team work was dedicated to define in a full expression of this quantity, and its promising performances compared to noble metals. In this specific case, carrier density in graphene is governed by their relaxation lifetime (τ) , Fermi velocity (v_F) and mean free path (λ).

A specific focus study was operated on chemical potential (μ_c) influence in order to be able to predict EM conductivity change in frequency under voltage bias conditions. Performances predictions from this numerical modelling tool help in the selection of technological processes parameters suitable for final device functionality in demonstrators (4).

$$\boldsymbol{n_S} = \frac{2}{\pi\hbar^2 v_f^2}\left[\int_0^\infty \boldsymbol{\varepsilon}\ \left(\boldsymbol{fd(\varepsilon-\mu_c) - fd(\varepsilon+\mu_c)}\right)\boldsymbol{d\varepsilon}\right] \qquad (2)$$

$$\boldsymbol{n_S} = \frac{2}{\pi\hbar^2 v_f^2}(\boldsymbol{kT})^2\left[\ -\boldsymbol{Li_2}\ \left(-\boldsymbol{e}^{\frac{\mu c}{kT}}\right) + \boldsymbol{Li_2}\ \left(-\boldsymbol{e}^{\frac{-\mu c}{kT}}\right)\right] \qquad (3)$$

$$VDC = \frac{4\,qetg\,(kT)^2}{\varepsilon r\varepsilon 0\,\pi\hbar^2 vf^2}\left[\ -\boldsymbol{Li2}\ \left(-\boldsymbol{e}^{\frac{\mu c}{kT}}\right) +\ \boldsymbol{Li2}\ \left(-\boldsymbol{e}^{\frac{-\mu c}{kT}}\right)\right] \qquad (4)$$

This mono/multilayered graphene analytic modelling allows the implementation of this material in fullwave analysis tools in 3D electromagnetic softwares as a complex-type sheet impedance defined as a specific “thickness-free” surface boundary condition, avoiding any intensive computing calculation needs for meshing along the critical nanoscale thickness of this material. Hence introduction of resistance and reactance provided by this material is achievable at circuit level, starting from complex resistivity definition, inversely proportional to complex conductivity defined in (1) and then integrated the overall material volume. A second step consists in the translation of this volume impedance into a sheet impedance as an independent quantity from thickness expressed in Ohms/squ, by a standard renormalization from thickness parameter.

From output results of this study, technological process steps identification is reachable by the determination of the realistic kinetic inductance which must be delivered by mono/multi graphene material under bias conditions for antenna design performances optimization by DC bias tunability. As reported in Figure 1, the choice of dielectric substrate thickness with respect to its relative permittivity is crucial to address low DC bias voltage levels for tunability.

From NANO RF project, a design choice of a serial metallic inductive compensation technique to capacitive MWCNT bundle behaviour has been validated, in order to fulfil the LC resonant device mandatory for antenna design. After several inductive structures studies in association with technological process, spiral-based configurations have been selected and led to the layout of 13 antenna designs. Circuit-based and 3D

electromagnetic co-simulations results have revealed achievable impedance matching and circuit resonance of emitting devices thanks to CNT bundle impedance contribution (Figure 2).

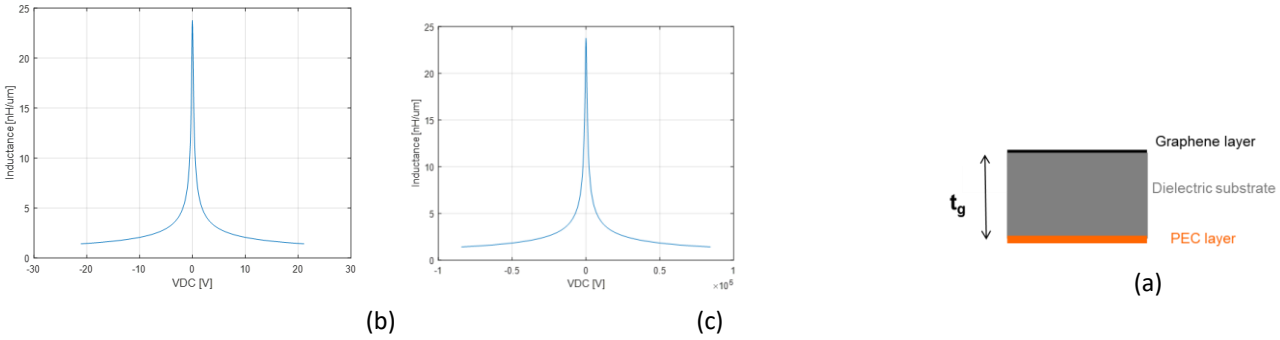

Figure 1 : Kinetic lineic inductance of a 10nm-thick graphene layer of 1cm² area deposited on a dielectric substrate under bias conditions: (a) Quartz substrate (ε_r= 3.4) with a thickness of 10 nm selection – (b) HR Si substrate with a thickness of 300 µm (c) cross section of the structure under study

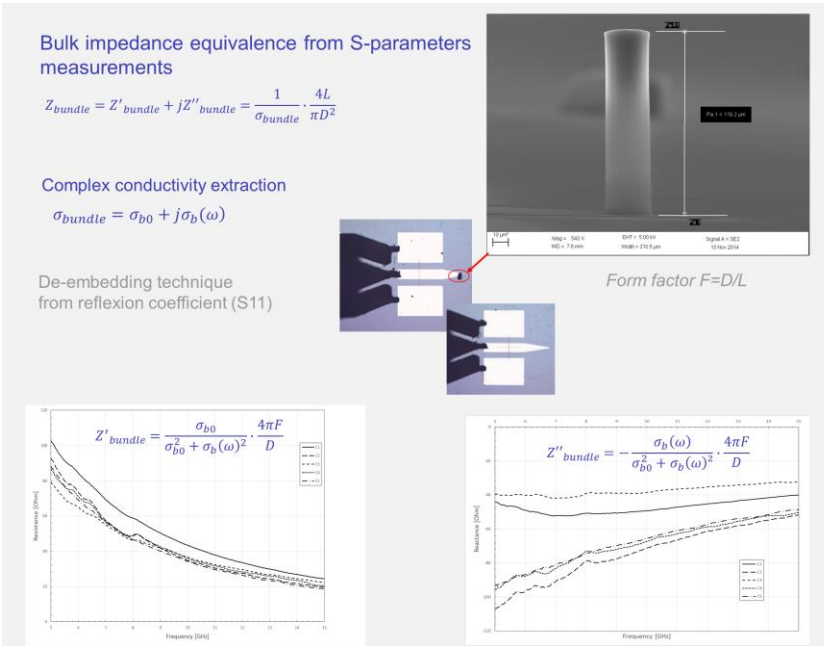

Figure 2: Experimental qualification of MWCNT bundles with form factor F (Diameter D and Length L)

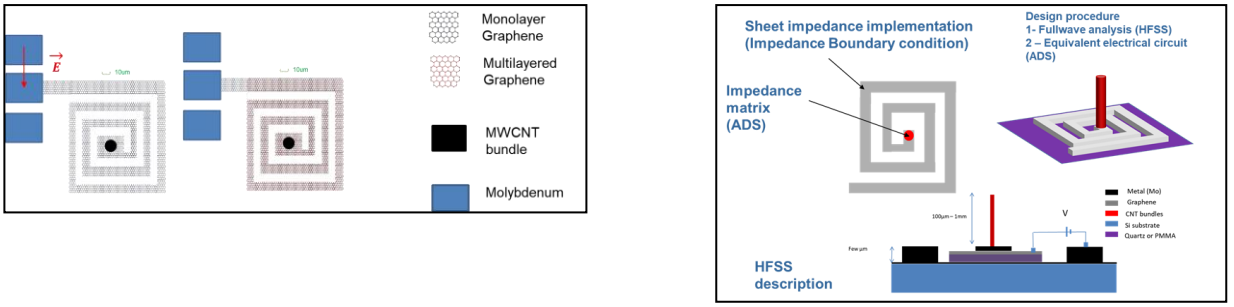

Figure 3: Top view of the targeted antenna design [patented] (left) and cross section description of NANOSMART graphene CNT based nano antennas embedded with design procedure.

These reference designs are now converted into graphene/CNT-based antenna design by enforcing inductive spiral part by a mono or multi layered graphene sheet with implementation of a thin dielectric layer for DC voltage bias application as in Figure 3.

➢ Reconfigurable CNT filters

The task is dedicated to the design of a tunable and reconfigurable filter based on carbon nanotubes (CNTs) displayed in Figure 4. The reconfigurability is given by the position of the three switches. The above filter is working in X band and can be a high –pass filter (HPF) , bandpass (BPF)filter or low-pas filter (LPF) depending how the switches 1-3 are positioned. When switches 1 and 3 are on and switch 2 are off, the circuit performs as a tunable low-pass filter; when switch 1 is off and switches 2 and 3 are on, we have a tunable high-pass filter. Finally, a band-pass filter is obtained when switches 1 and 2 are on and switch 3 is off. The integration of CNTs with FET based on 2D materials is within the concept of sequential integration planned in NANOSMART.

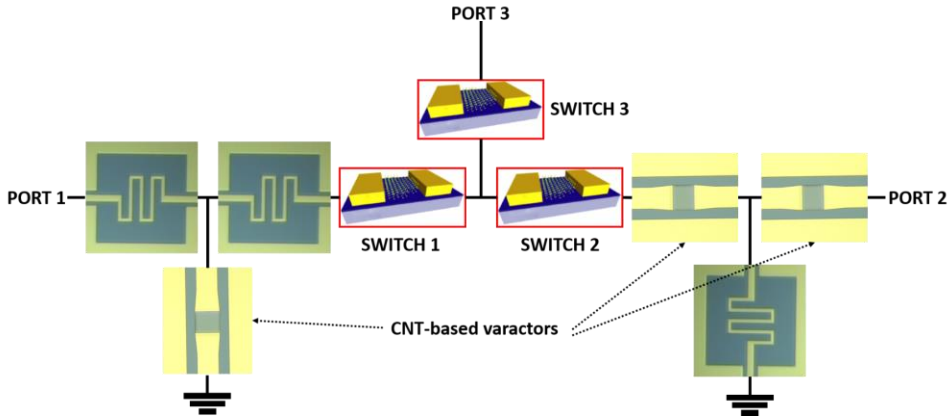

Figure 4 : CNT tunable and reconfigurable filter.

The tunability of the above filter is given by the CNT varactor – a vertical array of CNTs which are attracting via an applied DC voltage. The capacitance is varying in the range 0.05-2.2 pF, when the DC voltage is varied in the range 0-6.5V (see Figure 5).

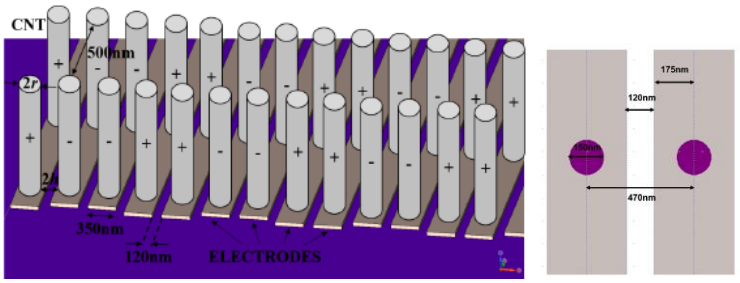

Figure 5 : CNT array varactor formed by CNTs grown vertically on interdigital structure (IDT) visible in the design of the filters .

➢ Sensors

○ RF sensors

We have designed and produced the masks (WP3) of the RF sensor. The RF sensor is a detector formed by antenna (bow-tie) integrated with a MIM (metal-insulator-metal) diode where the dielectric is HfO2 with thickness of few nm. The RF sensor is used to monitor RF power levels when the system is idle. This will provide information about incoming RF power density that is critical to establish the noise floor, implement wake up functions (super-regenerative Rx). We have made an analytical model of the MIM (see Figure 6) and we have extracted its nonlinear parameters for detection. Other parameters for design are :CPW gap = 60μm and CPW signal = 100μm, the total length of the signal is 608μm.the thin Pt layer is deposited on the HR Si/SiO2 layer.In every area configuration, *g*=1μm: it means that the Pt upper border is always 1μm above the MIM area.The MIM area is either 2x2μm^2 or 4x2μm^2 or 4x4μm^2.

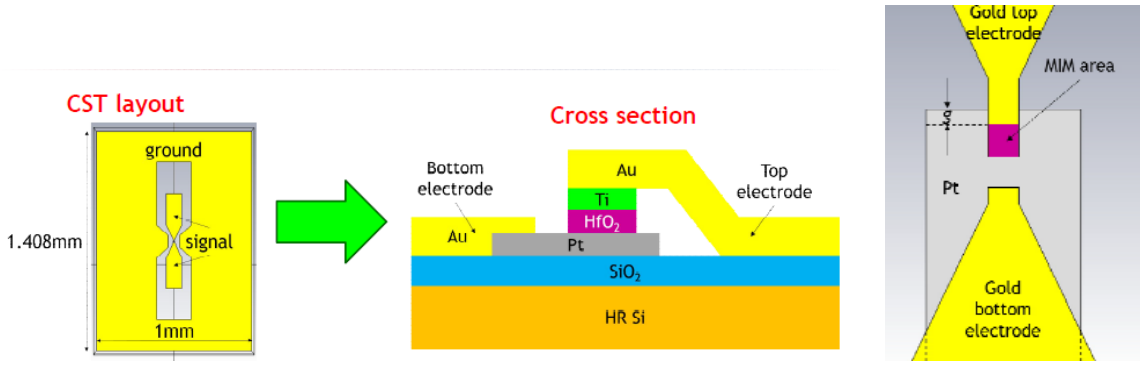

(a) **(b)**

Figure 6 : (a) The MIM diode (b) MIM diode integrated with the bow-tie antenna.

The performances of the detector were simulated and the results are (Figure 7):

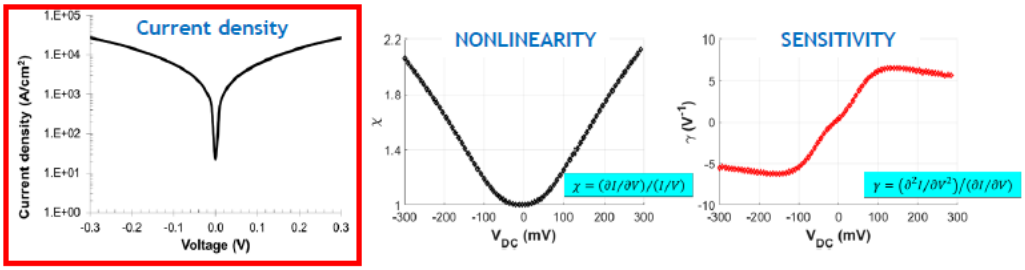

(a) (b) (c)

Figure 7 : The results of simulations (a) current density (b) nonlinearity (c) sensitivity

$\chi = 2.1$ at $\pm$ 0.3V, $\gamma = 6.42$ V^{-1} at $\pm$ 0.15V , thus we have a NEP of 471 pW/ Hz^{-1}.

○ Humidity sensors

The initial development of humidity sensor is based on MoS2/ different metal nanoparticles composite as sensing elements. The MoS2 nanosheet of 2 micrometer thickness is considered as a sensing element and its conductivity will change with respect to the humidity level. The interaction of water molecules on the surface of the sensing nanosheet will improve its conductivity. The sensing element is placed on top of the inter digitated electrodes with the channel size of 100 micrometer. A constant DC current of 1µA is applied between the terminals and measured its resistance change with respect to the humidity.

The initial simulation of the humidity sensor has been performed using COMSOL Multiphysics. Device geometrical details and the simulated structure are shown in Figure 8.

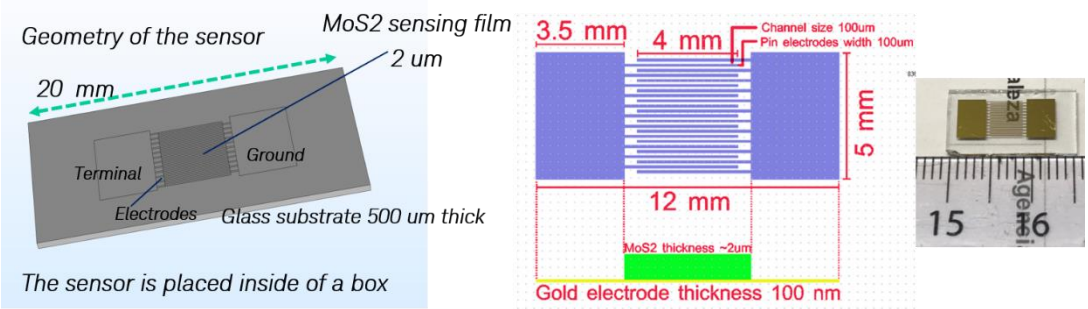

Figure 8 : Shows the geometry of the fabricated and simulated humidity sensor. Right end picture shows the fabricated sensor device.

The device contains both thin metal layers as well as the sensing film with respect to the big glass substrate. In order to maintain fine meshing of the device, the meshing has been done in three steps. Free triangular meshing and swept mesh is considered for the thin layers and then a free tetrahedral meshing is considered for the other surrounding structures and the air box.

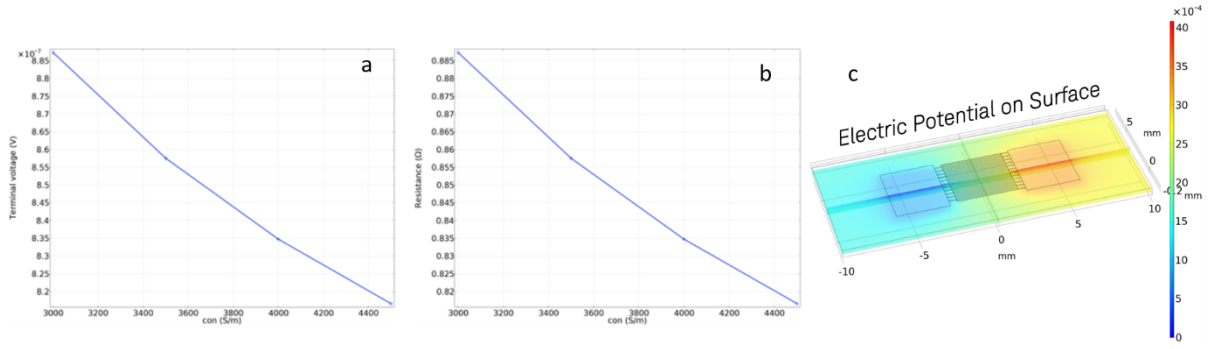

Figure 9 : (a) The terminal voltage with respect to different conductivity values of the sensing film, (b) the resistance change, (c) the distributed electric potential map.

Initially, a parametric simulation study has been performed by changing the conductivity values of the sensing film (from 3000 S/m to 4500 S/m) and the measured terminal voltage values and the resistance is shown in Figure 9. The conductivity values taken here was very high and the inclusion of the Cu/Ag nanoparticles has not been considered. The effect of the metal nanoparticles will be added with an artificial layer on top of the

sensing layer in the future simulations. All these effects will be considered to enhance the simulations to get matched results with experiments.

Fabrication activities

➢ CNT & 2D material supply

○ CNT Mechanical measurement

Since carbon nanotubes (CNTs) will be used as antennas, switches and filters in the Nanosmart project, the mechanical performance of the CNTs becomes critical in the project. Therefore, we measured the Young's modulus of the CNTs grown by our partner SHT.There are a few different methods to measure the mechanical performance of CNTs, such as measurement on bulk CNT bundles and on individual CNTs using atomic force microscope (AFM), transmission electron microscope (TEM), Raman spectroscopy or X-ray diffraction (XRD).[28]–[29] In this project, we used an indirect method in TEM machine to measure the crystallinity of CNTs and extracted their Young's modulus.[30] As it's well known, the crystallinity of CNTs is highly dependent on the in-plane crystallite size in the rolled graphene wall in CNTs. Therefore, we can firstly measure the crystallite size in the CNT wall and then link the crystallographic data to the mechanical performance of the CNTs. The CNTs are grown by thermal chemical vapor deposition (TCVD) method under 700 °C using Fe as catalyst and Al2O3 as diffusion barrier. First of all, we use selected area electron diffraction (SAED) in TEM to obtain the quantitative information about the average crystallite size in the CNT wall. The acceleration voltage is kept below 90 kV to avoid any potential damages on the CNT materials induced by the electorn beam and the base pressure is around 7×10-8 mbar during the measurement. TEM images of the as-grown CNT samples are shown in Figure 10, and the SAED pattern is shown in Figure 11. The position and width of the diffraction spots can provide the information about the interlayer distance between CNT walls. The spots in the ring-like pattern originate from the in-plane graphene structure in each CNT wall. Depending on the chirality of each CNT wall, there could be 6 or 12 spots on the ring. Since in this project the CNTs are multi-walled, a multitude of spots are observed in the pattern. Qualitatively a sharper ring pattern indicates a higher quality (less defects) of the CNTs.

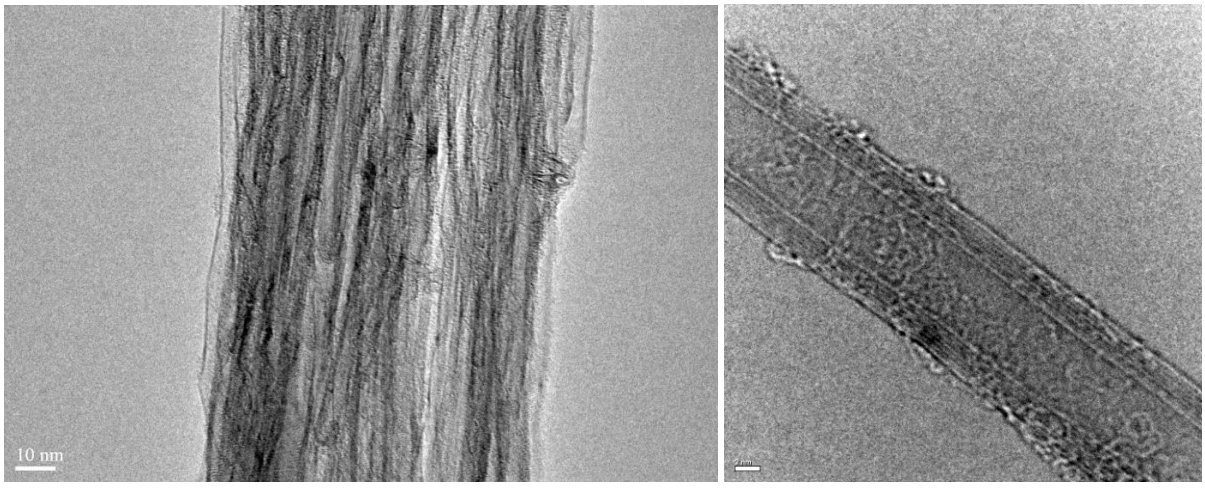

(a) (b)

Figure 10 : TEM images of the as-grown CNTs.

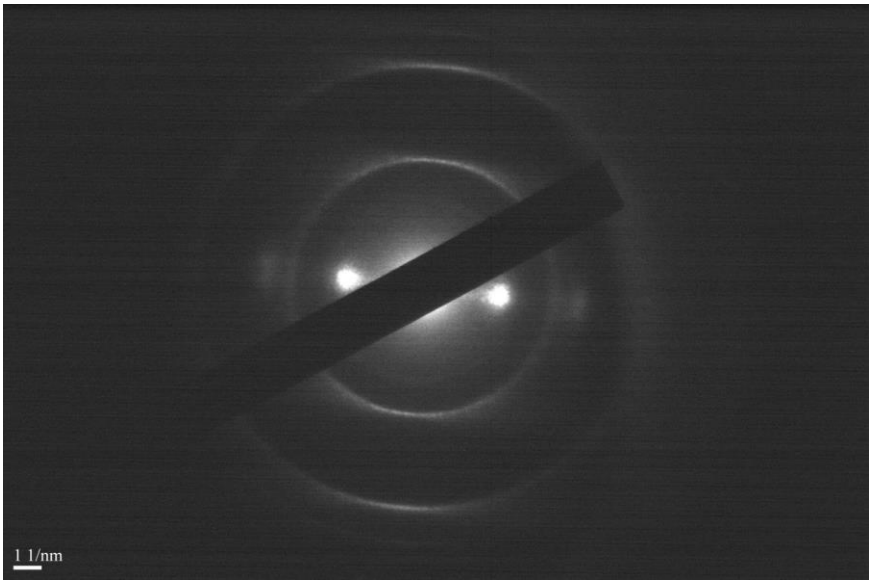

Figure 11 : SAED pattern of the as-grown CNT samples.

The crystallite size in the CNTs can be calculated by the Scherrer equation:

$$L = \frac{K \cdot \lambda}{\Delta(2\theta) \cdot \cos\theta}$$

Where K is the Scherrer constant, λ is the wavelength of the diffracted radiation, θ is the angle of diffraction and Δ(2θ) is the line broadening due to crystallite size measured in radians on a 2θ scale. Therefore, the crystallite size of the as-grown CNTs is 5.3 nm, which corresponds to a Young's modulus of 75 GPa, according to ref [7] (Figure 12).

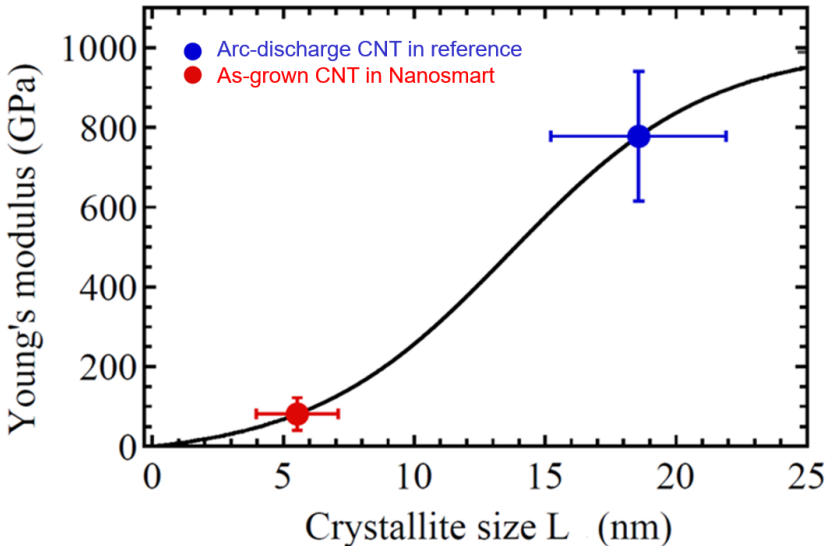

Figure 12 : Young's modulus E vs. crystallite size L. [7]

➢ CNT filters

Regarding the result of the design of the CNT filter and to improve the performance of the device, we have to increase the thickness of the metallization for the interdigit contact (IDT).

A optimization has be done as presented on Figure 13

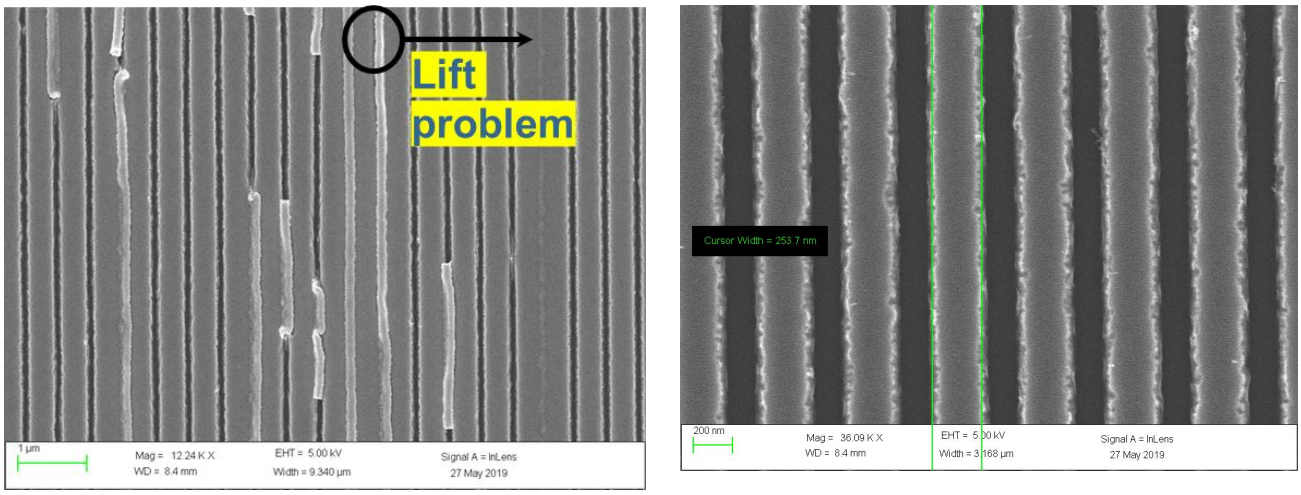

350 wide, 120 nm gap (100nm Mo thick)

250 wide, 200 nm gap (100nm Mo thick)

Figure 13 : Optimization of the thickness of IDT

Different wide and gap has been tested to obtain a digit of 100nm thick. As presented on Figure 13, for a gap of 120nm, it was difficult to completely remove the resist between the gap. We obtain the best result for a gap of 200nm.

After optimization, we have realized a CNT filter using the design from WP2 as presented in Figure 14

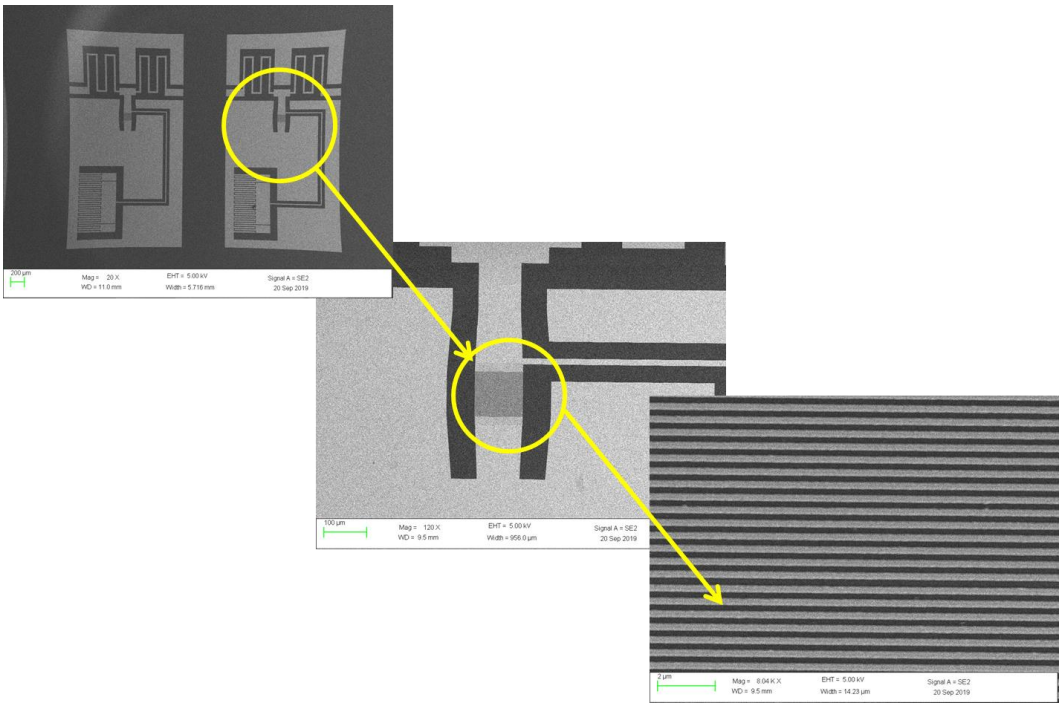

Figure 14 : Manufacturing of CNT filter

➢ CNTs/Graphene Antenna

Following the preliminary design of CNT antenna using a graphene layer as inductance, first test has been done to determine the new process flow. The first step is to validate the process parameter to etch the graphene layer to define the inductance. We know the graphene is very sensitive to the technological process and we have to find a process compatible with this material.
On **Figure 15**, we can see graphene layer made by SHT and patterned after lithography and RIE plasma.

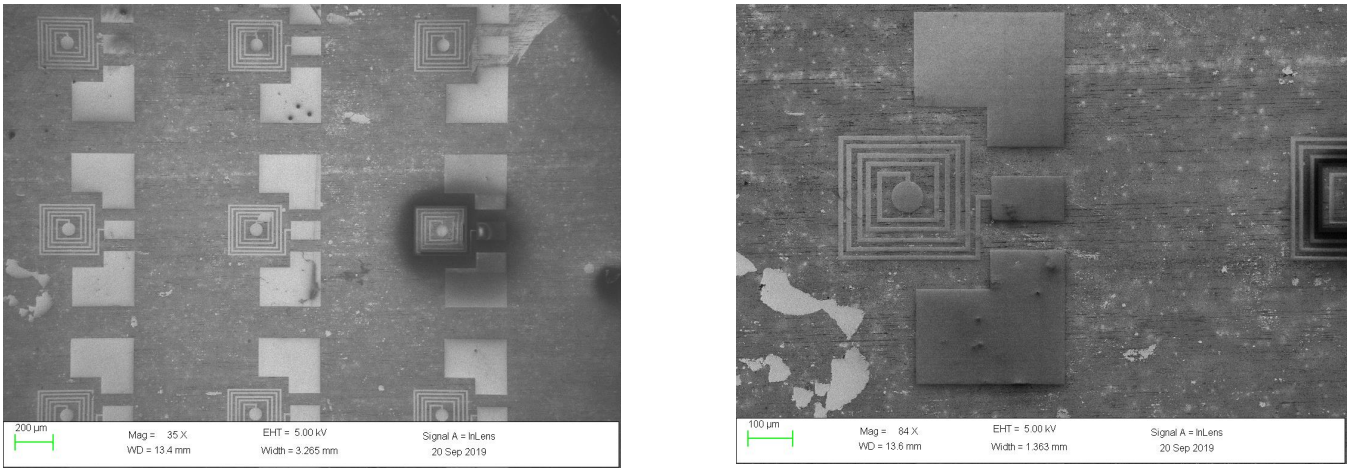

Figure 15 : patterning of graphene layer for CNT antenna

Another key point is the possibility to deposit a metal layer (corresponding to the coplanar line) on graphene layer. **Figure 16** show the result of litf off process (200nm of Mo) on graphene layer.

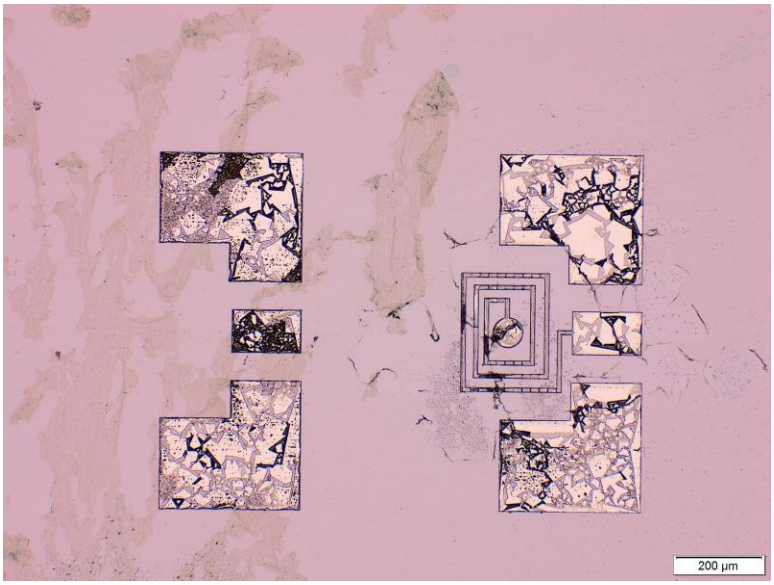

Figure 16 : patterning of graphene layer for CNT antenna

Poor adhesion of the metallization layer is observed on the graphene layer. Also the graphene in contact with the resist (apart from the metallization) has been removed during the lift off despite the fact of not having used ultra-sonic bath. Some new tests are ongoing with a annealing of graphene layer before to process the sample with the aim to improve the adhesion of graphene to the substrate.

Some process procedure and design modifications are under work to overcome fabrication constraints.

➢ Sensor Fabrication

Regarding the humidity sensor, we have developed a sensing platform based on transition metal dichalcogenides (TMDs) and metals nanoparticles composite active material. TMDs, such as MoS2 or WS2, have been identified as promising candidates for sensing application and nanoparticles of metals, such as Ag, Au and Cu, were added to improve the sensitivity and stability of the sensor. Incorporating Ag nanoparticles into inorganic semiconductors or polymers is an effective method for enhancing the function of materials. In humidity sensing, Ag nanoparticles were proven to be potential dopants that can increase the number of vacancies on the surface of humidity-sensing materials, resulting in more adsorption sites for water molecules.

Solution-exfoliated MoS2 and WS2 nanosheets were obtained using a sonicator probe system and nanosheets with different sizes were extracted by centrifugation and vacuum filtering.
On top of that, we have developed a modification process, in which the $CuCl_2$ and $AgNO_3$ were used in order to select MoS2 nanoparticles with different sizes. Metalic nanoparticles attached to MoS2 nanosheets increasing the precipitation rate. The large area MoS2 nanosheets (with more nanoparticles attached) precipitated into the bottom of the solution in room environment, while small size MoS2 flakes (with less nanoparticles attached) were suspended in the top solution, as shown in Figure 17. The TEM images confirmed that metal nanoparticles attach to the MoS2 nanosheets, both in the top solution and the bottom precipitate. The adhesion is strong and the nanoparticles stay attached even after mild sonication treatment.

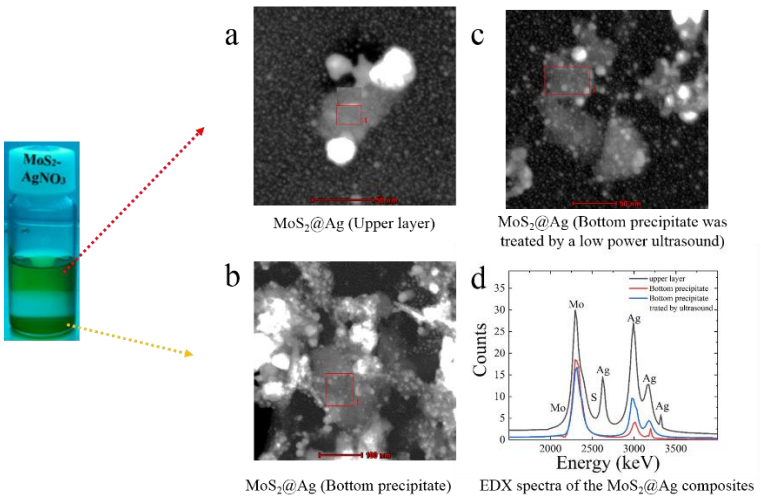

Figure 17 : STEM images of the composite of MoS2 nanosheets and silver nanoparticles (a) the lighter composite of MoS2 nanosheets and silver was extracted from the upper layer solution, (b) the heavier composite of MoS2 and silver come from the bottom precipitate, (c) the bottom precipitate was treated by a low power ultrasound, and big size silver nanoparticles and MoS2 nanosheets are separated.

Characterization activities

➢ 2D material characterization

In addition to aforementioned characterisation of samples HS1, HS2, HS3, HS4, HS5, HS6, HS7, PS1 and MoS2 by Micro Raman, Far IR, TEM and SEM TNI have work toward developing a methodology for material characterising of 2D materials. TNI found that literature reference material data on HfS2 is scarce and purchased two single-crystal HfS2 (See Fig. 17) from two EU suppliers (HQ Graphene from Netherlands and Ossila from UK).

Figure 17 (a). HfS2 single-crystal HQ Graphene (Netherlands) (b) HfS2 single-crystal Ossila (UK)

In addition to acquiring reference data TNI have investigated air exposure effects that are critical for device fabrication. HfS2 crystallizes with octahedral metal coordination in the 1T polytype. The space group is P3m1 (trigonal) and Group symmetry analysis indicates that lattice vibration in this structure has 6 normal modes :

$$\Gamma = A_{1g}(R) + E_g(R) + 2A_{2u}(I) + 2E_u(I)$$

The Micro Raman measurements acquired with two excitation wavelength (455nm and 514nm) are shown in Figure 18.

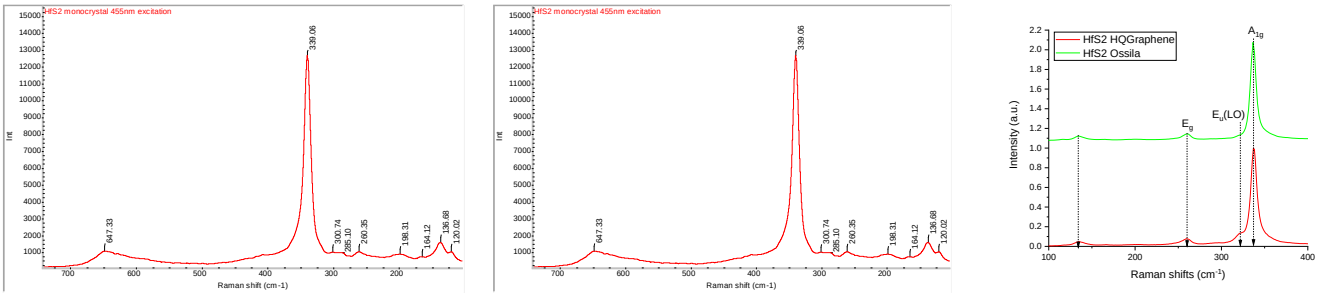

Figure 18 : Micro Raman measurements on HfS2 single-crystals: left, 455nm laser excitation, middle, 514nm laser excitation and right a comparison between the two HfS2 single-crystals.

TNI have cross-checked the 514nm Raman measurement with measurement done on TRT Micro Raman and obtained and excellent agreement. The results are summarised also in Table 1. Additional phonon modes are observed that can be associated to either presence of point defects or with changes due to the air exposure.

Table 1 : Summary of Raman results on HfS2 single-crystals

SOTA- λ=514nm (cm^{-1})	λ=514nm (cm^{-1})	λ=455nm (cm^{-1})	Assignment
-	-	120	?
-	135	136	?
-	166	164	E_u(TO)
-	203	198	?
260	260	260	E_g
-	-	300	?
321	321	-	E_u(LO)
337	337	339	A_{1g}
645	651	647	2xE_u(LO)

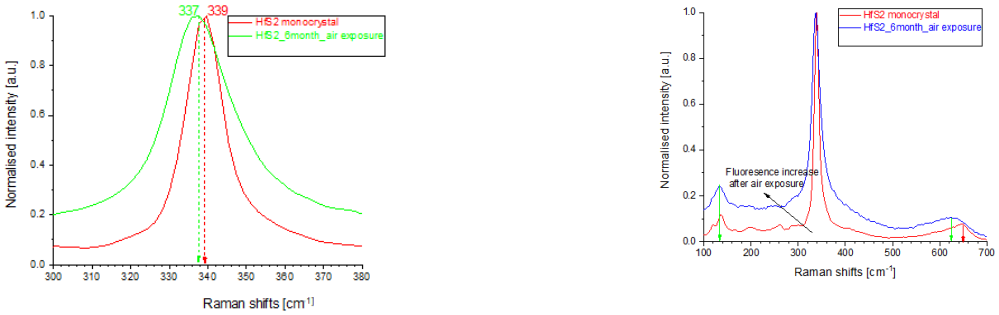

Figure 19 : The impact to air exposure on HfS_2

In Figure 19 are shown the Raman spectra for HfS2 single-crystal after air exposure. The impact of air exposure on HfS2 is more severe than in the case of MoS2. This means the 2D HfS2 films will require in-situ passivation immediately after the growth with a Al2O3 layer.

Finally, we have investigated the methodology for assessing the uniformity of 2D material on large substrates (4-inch). TNI explored the potential of spectroscopic ellipsometry and use as case study a few-layer MoS2 grown by TNI on a 4-inch Si wafer. In Figure 20 are shown the spectroscopic experimental data along with the model data fits, the extracted optical constants for few–layer MoS2 and the thickness mapping results across the 4-inch substrate. The first results indicate that spectroscopic ellipsometry potential as metrology tool for the qualification of 2D materials on large substrates.

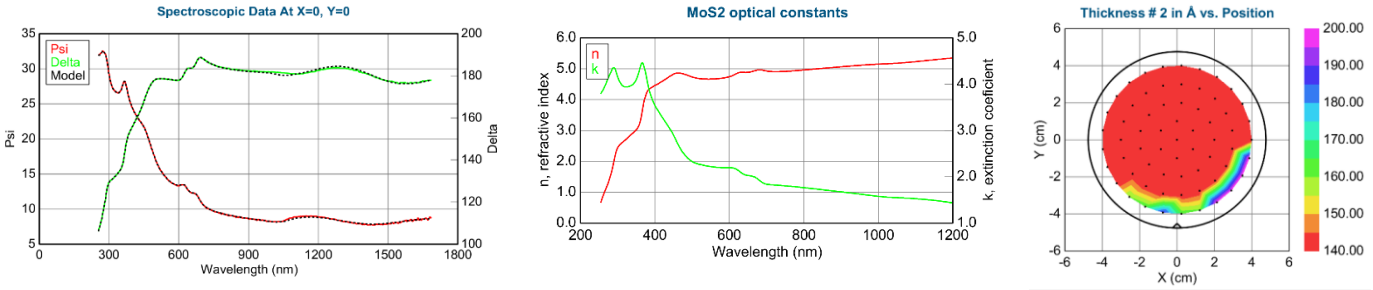

Figure 20 : Spectroscopic Ellipsometry mapping of few–layer MoS2 on a 4-inch Si substrate. Left, the spectroscopic experimental data along with the model data fits; middle the first report of optical constants for few–layer MoS2 and right the thickness mapping results across the 4-inch substrate.

➢ Humidity sensor characterization

When the solution was heated to 100°C a floating MoS_2 - metal ions membrane was formed on the surface of solution, which had a foam-like structure. We used the floating membrane as the sensing material, which was placed on top of the interdigitated gold electrodes on a glass substrate (Figure 21a).

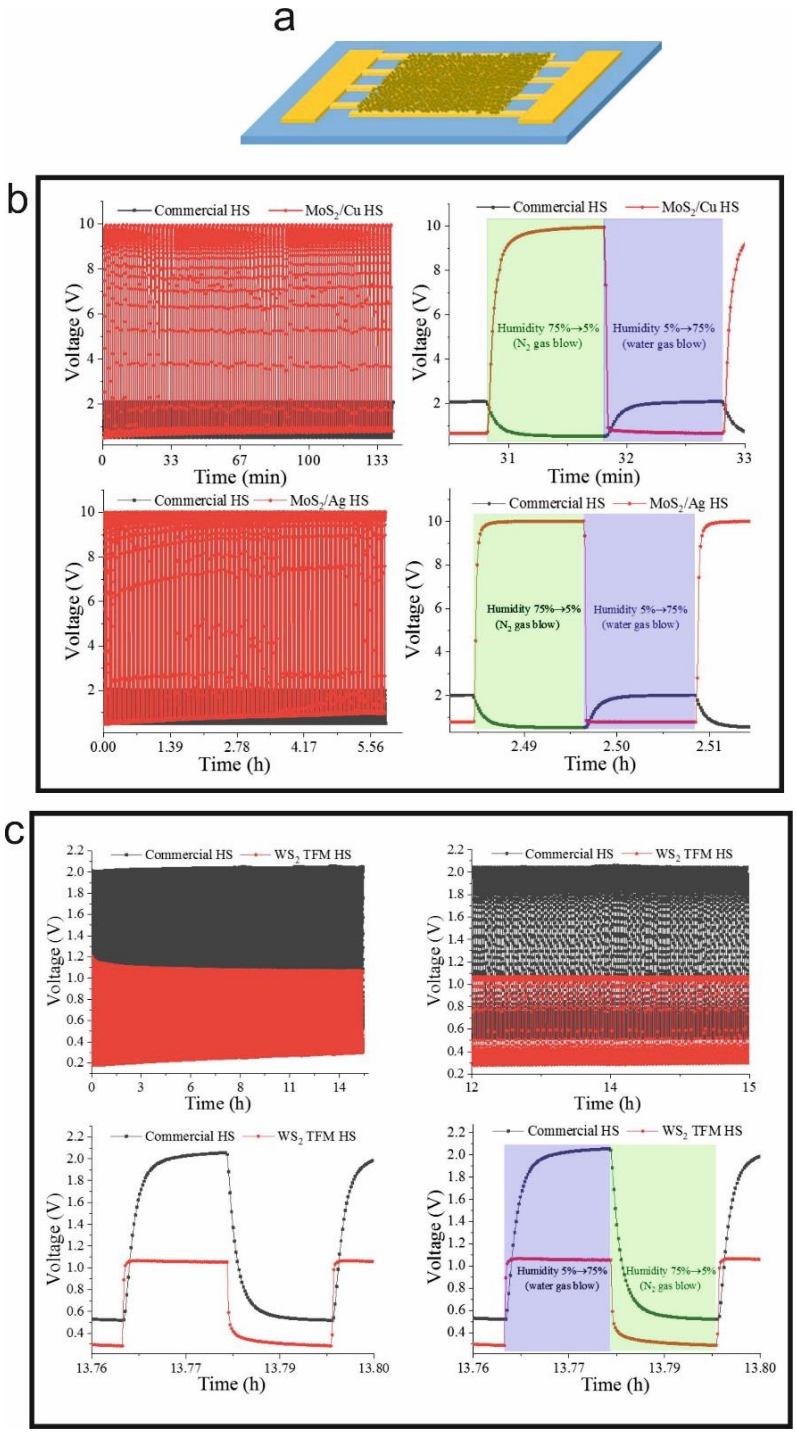

Figure 21(a) Schematics and performance of humidity sensor based on (b) MoS2-Ag (c) MoS2-Cu at applied current of 1 μA

MoS_2 nanosheets with smaller sizes show better humidity sensing behaviour than the original MoS2 nanosheets without filtering and centrifugation, mainly due to their higher surface-to-volume ratio. We have also observed different resistance response to humidity between the MoS2 and WS2. Finally, the influence of metal nanoparticles on the sensing capabilities was studied.

In order to test the RH sensors, we have designed and built a humidity chamber operating at room temperature. Humidity sensors with different nanosheet sizes were assembled and tested against the commercial humidity sensor (HS1101LF, TE Connectivity). Constant current was applied to the devices and

the output voltage was registered. The devices showed good response to RH in the range of 5 - 75%. Moreover, they show excellent stability and faster time response than the commercial device.
Figure 21 (b) shows the voltage response of $CuCl_2$ and $AgNO_3$ decorated MoS_2 nanosheets as function of time. The square voltage response corresponds to a cyclic pumping of the gas flow of water in the chamber. The sampling frequency is 0.82s per point. In the first column the two graphs show the excellent repeatability of the two sensors after a few thousand cycles. The response/recovery times of the MoS_2/Cu sensor and MoS_2/Ag sensor are about 8s/1s and 3s/1s, respectively. Here, it is noticeable that the MoS_2/Ag sensor shows better performance than the MoS_2/Cu sensor.

We also investigated the humidity sensing behaviour of WS_2 nanosheets using the same fabrication and characterization methods as described before. As shown in Figure 21 (c) WS_2 nanosheets-based humidity sensors show excellent repeatability after working over 15 hours. We fabricated three types of WS_2–based RH sensors base on: floating membranes, precipitate, and a composite with MoS_2. All of these sensors show the same repeatability (>15 h), and their response/recover times are about 1s/1s, 8s/6s, and 1.5s/2s, respectively. It is worth mentioning that compared with MoS_2 nanosheets-based humidity sensors, WS_2 nanosheets-based humidity sensors show different working mechanism, and their output voltage increased with the ambient humidity.

NanoSmart Publications

In the last 12 months, the partners of the NanoSmart project published various results related to the project.

- M. Aldrigo, M. Dragoman, S. Iordanescu, A. Dinescu, D. Vasilache, I. Povey, M. Modreanu, “Microwave detection with MoS_2-based self-switching diodes,” 42nd International Semiconductor Conference (CAS), 9-11 October 2019.
- M. Aldrigo, M. Dragoman, S. Iordanescu, D. Vasilache, A. Dinescu, M. Shanawani, D. Masotti, “Graphene diodes for 5G energy harvesting: design, simulations and experiments,” Proc. of the 49th European Microwave Week Conference, 29 Sep.-4 Oct. 2019, pp. 37-40, 2019
- Andreas Nylander, Marlene Bonmann, Andrei Vorobiev, Josef Hansson, Nan Wang, Yifeng Fu, Johan Liu. RF Properties of Carbon Nanotube / Copper Composite Through Silicon Via Based CPW Structure for 3D Integrated Circuits. IEEE Nanotechnology Materials and Device Conference 2019, Sweden. pp 1-5.
- L. Pierantoni, “Bridging the Gap between Electromagnetic and Quantum Transport in the Analysis of Nanomaterials based Devices”, Invited Talk at the International Conference OptoX-NANO, Okayama, Japan, 2-4 Dec. 2019
- M.Modreanu, A.Ziaei, “NANO components for electronic SMART wireless systems”, OptoX NANO 2019, Europe-Japan Networking Special Session, December 2019, Okayama, Japan.
- P.Xiao, M.Sledzinska, C.M. Sotomayor Torres, “Fast-Response Humidity Sensor Based on Transition Metal Dichalcogenide Nanosheets and Metal Ion Composites”, Poster presented at Material Research Society (MRS) Fall Meeting 1-6/12/2019 in Boston, Massachusetts
- P.Xiao, M.Sledzinska, C.M. Sotomayor Torres, “Fast-Response Humidity Sensor Based on Transition Metal Dichalcogenide Nanosheets and Metal Ion Composites”, Poster presented at International Winterschool on Electronic Properties of Novel Materials (IWEPNM), 9 16/03/2019, Kirchberg, Austria
- M.Sledzinska, Poster at European Researcher’s Night presenting activities of ICN2 in the framework of NANOSMART project, 27/09/2019 Cosmocaixa, Barcelona, Spain

Remember to visit us at :
http://project-nanosmart.com/

NanoSmart is a project co-funded by the European
Commission under the H2020 program
Grant Agreement N°: 825430

Contact:

Dr. Afshin Ziaei, NanoSmart Coordinator
mailto:afshin.ziaei@thalesgroup.com